Ionic liquids assist synthesis of Ag/AgX (X = Cl, Br, & F)-decorated rGO for visible light photocatalytic applications

K. Lakshmanamoorthy[1] and S. Manivannan[1,*] (iD)

[1] *Carbon Nanomaterials Laboratory, Department of Physics, National Institute of Technology, Tiruchirappalli 620 015, India*

ABSTRACT

Three different ionic liquids based on 1-butyl-3-methylimidazolium were prepared and used to synthesize Ag/AgX (X = Cl, Br, & F) nanoparticles-decorated reduced graphene oxide (rGO). The formation of the Ag/AgX-rGO composites were confirmed from the powder XRD patterns of the samples and the absorption peaks at 220 nm, 280 nm, and 352 nm in UV–visible spectroscopy. The functional groups in rGO and decoration of Ag/AgX on rGO sheets were established by the peaks in FT-IR at 1192 cm^{-1}, 1270 cm^{-1}, and 1569 cm^{-1}. The I_D/I_G ratios in micro-Raman analysis, and FE-SEM images witness the above observation. The endothermic peak at 956 °C in DSC analysis indicates the presence of silver in the samples. The natural visible light photocatalytic properties of these materials were studied with the degradation of methylene blue (MB) dye. The samples with Ag/AgX structures have better photocatalytic properties than AgX and rGO. This is due to the increased utilization of sunlight by the plasmonic Ag in the Ag/AgX-rGO samples and the fast charge separation by rGO. The samples GIA1 and GIA3 are showing better dye degradation efficiency, these samples degrade 97% and 97.5% of MB dye, respectively. The formation of AgX was dependent on the type of ionic liquids used in the synthesis which is highly reflected in the photocatalytic behavior.

1 Introduction

Industrial waste, especially the dyes from the textile industries, adversely affects the aqueous environments. Photocatalytic materials act as a catalyst to degrade the dyes by absorbing the light radiation. Dyes should be degraded before it enters the environment, which has been done by the photocatalytic materials. Semiconductors, like TiO$_2$, ZnO, ZnS, Fe$_2$O$_3$, SnO$_2$, etc., are widely explored photocatalytic materials, and among them TiO$_2$ is being considered as the prime candidate due to its low cost, environmental friendliness, and high stability [1]. TiO$_2$ is a wide bandgap material with a bandgap of about 3.2 eV. Hence, it requires an excitation source

Address correspondence to E-mail: ksmani@nitt.edu

of wavelength less than 400 nm to create electrons in the conduction band and holes in the valence band. This excitation wavelength falls in the UV region of the electromagnetic spectrum, so there is a huge requirement to design the active photocatalyst in the visible region of the solar spectrum. Most of the semiconductor-based photocatalysts have similar problems alike TiO_2 [2].

For their high visible light sensitivity silver halide-based semiconductors have been used as a visible light photocatalyst. Silver halides are highly active to the visible light but are unable to control the electron–hole recombination before it reaches the catalysts surface to get involved in the degradation process. Even though it possesses high visible light sensitivity, degradation of the catalyst during the photocatalytic process is a limitation. To reap more solar energy, metal-based plasmonic photocatalysts were designed which work by the principle of surface plasmon resonance (SPR). SPR is the collective oscillations of free electrons in metals by absorbing light radiation. The plasmonic metal nanoparticles act as an alternative type of sensitizer to light absorption to enhance photocatalytic ability. To improve the photocatalytic activity of the AgX-based materials, Ag/AgX (X = Cl, Br, & F) heterostructures-based catalysts were designed. Ag/AgX materials drastically improve the activity by SPR effect as well as limited the e^-, h^+ recombination by separating the charges. Recently, many reports are available with Ag/AgX nanostructures-based photocatalytic applications. Photocatalytic efficiency was improved by tuning the morphology of the prepared catalysts and through doping [3, 4]. The AgX visible light-responsive plasmonic materials were also used to convert the CO_2 into useful fuel like methanol through the photocatalytic reduction process [5]. The bandgap of the $AgCl_xBr_{1-x}$ samples is tuned by changing the composition of X in the AgX (X = Cl, Br, & F) which improves the photocatalytic property of the material [6–8]. By changing the halide compositions in the Ag/AgX (X = Cl, Br, & F) systems, one can modify the bandgaps, which enables the materials to work in different redox potentials. These systems will be used to decompose the various organic pollutants. This encourages us to modify the compositions of the halide ions in the silver halides to change their physicochemical properties towards photocatalytic applications.

Meantime, graphene oxide (GO) has received extensive attention towards the synthesis of inorganic nanomaterials, due to its flexibility and availability of oxygen functional groups (hydroxyl, epoxy, and carbonyl). The oxygen functional groups act as nucleating sites for the growth of inorganic nanoparticles and modify the size and shape of the nanoparticles. Apart from this, reduced graphene oxide (rGO) has excellent charge transport properties that enable fast charge separation, which is an important parameter in the photocatalytic process [9–12]. The 2D structure of rGO has enhanced the dye absorption capabilities of the photocatalytic materials as well as the stability of the catalytic materials. Recently, many groups have reported the AgX-GO/rGO-based nanomaterials towards photocatalytic applications [13–17]. In this work, we have used the microwave (MW)-assisted rapid synthesis method to prepare the Ag/AgX-rGO composites. MW-assisted synthesis methods are more effective than conventional methods, and it reduced the reaction time. The rapid supply of heat energy enables reactions that are not possible in conventional methods.

On the other hand, usage of Ionic liquids (ILs) to synthesize nanomaterials have been increased in recent times because of its properties like insignificant vapor pressure, low toxicity, high ionic conductivity, high thermal and chemical stabilities, and decent solubility in various solvents [18]. Plenty of room-temperature ILs are available and based on the requirement specific ILs can be designed by changing their constituent ions. Among the thousands of task-specific IL combinations, imidazolium-based ILs are widely used in various applications. 1-butyl-3-methyl imidazolium ($BMIM^+$) cation-based ILs were used to synthesize silver nanoparticles with different morphologies, and it was found that the structure of the nanoparticles depends on the type of anion used and the cation chain lengths in the ILs [19, 20]. BMIM $FeCl_4$ was used to prepare Ag@AgCl core–shell structure and its visible light photocatalytic efficiency towards the degradation of methyl orange and 4-chlorophenol were studied. The anion of IL ($FeCl_4$) interacts with the surface of silver atoms and used to form the AgCl shell over the silver nanowires [21]. Imidazole-based ILs interact with the graphene structures by imidazole ring through cation–π electrons in graphitic structures. Further, ILs-rGO composites were used in the fields of sensing, electrochemical, and energy-related applications

[22, 23]. Based on the above literature, it is understood that ILs were used to modify rGO structures by the interaction with cations and the silver nanoproducts by the anions. By using different anions-based ILs one can tune the compositions of the halides in the AgX system, it modifies its physical properties. This motivates to use ILs to prepare and study the Ag/AgX-rGO composites, their applications towards the degradation of organic dyes. Here, we prepared Ag/AgX-rGO composites by using three ILs based on $BMIM^+$ cation with three different anions. The rapid MW irradiation method was used to prepare the composites, and the visible light photocatalytic degradation efficiency of the composites towards the degradation of methylene blue (MB) dye was studied.

2 Experimental methods

2.1 Synthesis of ionic liquids and GO

Imidazolium-based ionic liquids like 1-butyl-3-methylimidazolium tetrafluoroborate ($BMIM^+BF^-_4$), 1-butyl-3-methylimidazolium trifluoroacetate ($BMIM^+$ TFA^-), and 1-butyl-3-methylimidazolium methyl sulfate ($BMIM^+$ $MeSO_4^-$) were synthesized adapting the procedure reported elsewhere [24, 25]. GO was synthesized by using the modified Hummers method [26].

2.2 Synthesis of AgX/rGO composites

Solution A: 50 mg of GO was taken in 50 mL of ethylene glycol (EG) (EMPARTA®, Merck Life Science Private Limited, 99%) and sonicated for 1 h. Solution B: 47 mg of silver nitrate (EMPLURA®, Merck Life Science Private Limited, 99%) was taken in 20 mL (0.014 M) of EG and stirred for 1 h. Solution C: 155 mg of PVP (MW-55,000, Sigma Aldrich) was taken in 20 ml of EG along with 1.5 mg of NaCl (Analysis GR, Merck Specialties Private Limited, 99.5%) and 1.5 mg of KBr (IR spectral grade, Uvasal®, Merck KGaA) and stirred for 1 h at 80 °C. The solutions B and C were added with solution A and stirred for 5 min then the solution was kept in a household MW oven for heat treatment. The MW treatment was done for 2 min at 700 W power, then 360 W power with a break time of 2 min. Then, they were washed with DI water and ethanol several times

by centrifugation at 5000 rpm for 15 min, then dried at 60 °C for 8 h. The prepared sample was named as GIA1, the same procedure was followed for the other three samples except the ILs were added before the MW irradiation. The ILs used to prepare the composites were $BMIM^+$ BF_4^-, $BMIM^+$ $MeSO_4^-$, and $BMIM^+$ TFA^-, and the prepared samples were named as GIA2, GIA3, and GIA4, respectively. The samples were used for further studies.

2.3 Photocatalytic degradation of methylene blue dye

100 mL of the MB (Methylene blue stain, Merck Life science Private Limited) solution with a concentration of 5 mg L^{-1} was prepared, and 5 mg of the prepared samples Ag/AgX-rGO was added to it. Then the solution was kept in the dark environment for 30 min for the adsorption–desorption equilibrium of dye molecules on the surface of the catalyst. The solution was kept in sunlight with stirring for every 30 min and 2 mL of the solution was taken and centrifuged to remove the catalytic material. The supernatant was collected, and UV–visible absorption spectra (Shimadzu UV 2600) were recorded to find the degradation of the MB dye.

3 Results and discussion

The powder XRD patterns of the synthesized samples are shown in Fig. 1 (Rigaku Ultima III, 2° min^{-1} with a step of 0.02°). GO shows the peak at 11.2° corresponding to the (001) plane. For GIA1 and GIA3, both the FCC phases of Ag and AgX are present. The peaks corresponding to the angles 38.4° (111), 44.5° (200), 64.8° (220), 77.7° (311) are for the FCC structure of silver (matched with the JCPDS Card No: 04-0783) and the patterns at angles 27.6°, 31.9°, 45.5°, 56.6°, 66.3°, 75.4° correspond to the FCC phase of Ag(Cl, Br) (matched with the JCPDS card No:14-0255). Samples GIA2 and GIA4 show the peaks at angles 26.9° (111), 31.3° (200), 44.6° (220), 55.3° (222), 64.9° (400), and 73.6° (420) are for the cubic phase of AgBr (JCPDS card No: 06-0438). The peaks are shifted to the lower angle in the samples GIA2 and GIA4, which are due to the fluorinated AgBr, and leads to the formation of AgX (Br & F) [27]. No separate peaks were observed to the presence of AgF in these samples. The formation of AgX (Br & F) is explained by the anion
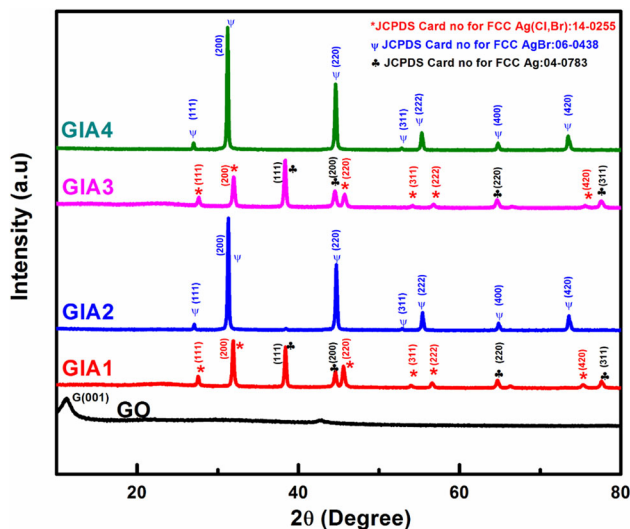
Fig. 1 Powder XRD patterns for the prepared samples

Fig. 2 UV–visible absorption spectra

exchange reaction that happed between the silver nitrate and the respective ILs. Pure Ag phase is disappeared in the samples GIA2 and GIA4, due to the conversion of Ag into AgX by a surplus supply of halide ions from the ILs. In the case of GIA1 and GIA3, both the phases are present.

In the presence of ILs $BMIM^+$ BF_4^- and $BMIM^+$ TFA^-, the peaks corresponding to pure Ag disappeared due to the anion exchange reaction taking place between the ILs and the NO_3^- ions of the $AgNO_3$. The anions of BF_4^- and TFA^- were exchanged after adding NO_3^- ions to form $BMIM^+$ NO_3^-. The native anions from ILs have interacted with Ag and then it separated into its constituent ions leading to the formation of AgX nanoparticles [28]. In the case of $BMIM^+$ $MeSO_4^-$ (sample GIA4), the anion exchange has not happened, which is reflected in the yields of the GIA samples as 60 mg, 93 mg, 55 mg, and 94 mg, respectively, for GIA1, GIA2, GIA3, and GIA4. This is due to the difference in the anion exchange interaction energy and the cation of the ILs used in the reactions [29, 30].

The UV–Vis (Shimadzu UV2600, ethanol) absorption spectrum (Fig. 2) of GO shows a peak at 220 nm corresponding to $\pi - \pi^*$ transitions of aromatic C–C bonds, and the small hump around 300 nm is for the $n - \pi^*$ transitions of C=O bonds [31]. For the samples, GIA1 and GIA4, the peak that appeared at 352 nm corresponds to the SPR of the Ag. With the emergence of this peak in the GIA1 and GIA3, one can confirm the formation of Ag/AgX structures. This peak disappeared in GIA2 and GIA4 indicating
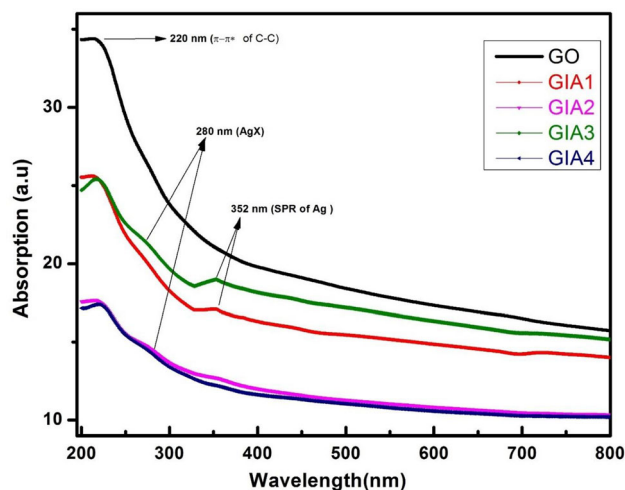
the absence of Ag metal. These results are consistent with the powder XRD results. The peaks at 280 nm correspond to the silver halides [32].

FT-IR spectra (Nicolet iS5 spectrometer, KBr pellet method) of the samples are shown in Fig. 3. The peaks at 1039 cm^{-1} (C–O), 1610 cm^{-1} (C=C), 1717 cm^{-1} (C=O), and 3350 cm^{-1} (O–H) are for the oxygenated functional groups in the GO. For the other samples, the peak corresponding to C=O is red-shifted to a higher wavenumber of 1725 cm^{-1}. The peak at 1643 cm^{-1} corresponds to the C=O in PVP due to the Ag/PVP interaction and the actual peak in pure PVP is at around 1660 cm^{-1} [33]. The peak for scissoring vibrations of the CH_2 group appeared at 1423 cm^{-1}. The peak corresponding to the C–N bond
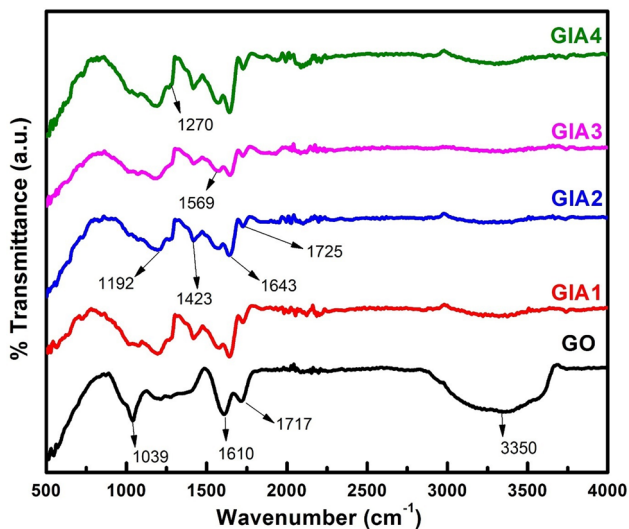

Fig. 3 Overlay of FT-IR spectra of GIA samples

in PVP is typically observed at 1283 cm^{-1}, for the Ag/AgX-rGO shifted to 1270 cm^{-1}. Both the peaks of C–O and C–N are shifted from their actual positions due to the formation of coordination bonds between silver atoms and the oxygen and nitrogen atoms from the PVP polymers [34].

The micro-Raman spectra (LabRAM HR Evolution Raman spectrometer, 532 nm, 50 mW) of the prepared samples are shown in Fig. 4. GO has the two characteristics peaks for graphitic structure centered around 1357 cm^{-1} (D band) and 1591 cm^{-1} (G band) [35]. The I_D/I_G ratio is found to be smaller for the samples GIA1, GIA2, and GIA3 compared to GO, which is due to the reduction of GO in these samples. The peak broadening and the positional shift in the D and G bands are due to the formation of metal–rGO bonds through oxygen functional groups. The new bands are around 1250 cm^{-1} (D*) and 1500 cm^{-1} (D**) in GIA3, D* corresponding to the sp^3 like defects, and D** for the C–H vibrations of hydrogenated carbons, respectively [36]. The band appeared at 995 cm^{-1} is for the S–O stretching vibrations, this S–O moiety was from the BMIM MeSO$_4$ IL.

The D and G band positions and the I_D/I_G ratio of the samples are shown in Table 1. The D band shifts to the lower wavenumber in the GIA composites compared to the GO, which indicates the modifications in the structure. The sample GIA2 has the lowest I_D/I_G ratio it results from the presence of less defected rGO.

FE-SEM images of the prepared samples are shown in Fig. 5, (ZEISS EVO 18). From the figures, one can
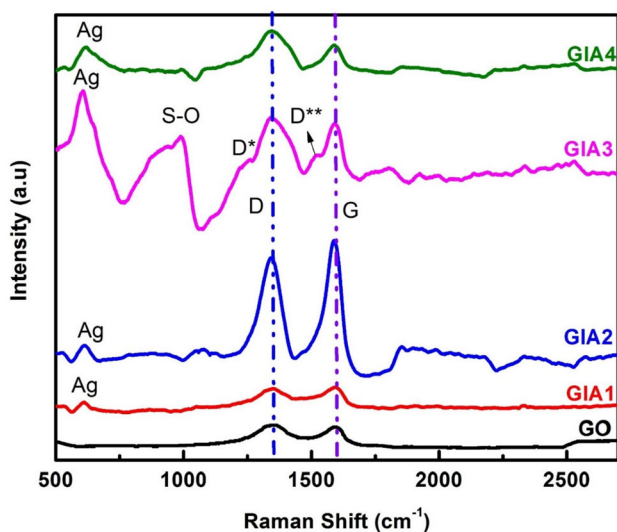
Table 1 D and G band positions and I_D/I_G ratios of the prepared samples

Sample	D (cm^{-1})	G (cm^{-1})	I_D/I_G
GO	1357	1591	1.158
GIA1	1346	1596	0.952
GIA2	1342	1586	0.871
GIA3	1340	1592	1.104
GIA4	1343	1590	1.546

find the sheet-like morphology of GO. The other samples show the Ag/AgX nanoparticles decorated on the rGO sheet. In GIA2, the particles were evenly distributed over the rGO sheets. In the case of GIA1, 2, & 4, the particles agglomerated at the edges of rGO sheets. These results are consistent with the micro-Raman results, the sample GIA2 has the lowest I_D/I_G ratio compared to other samples.

Thermogravimetric analysis was carried out in the nitrogen atmosphere (100 mL min^{-1}) in the temperature range from 30 to 1200 °C at a heating rate of 20 °C min^{-1} (TA instrument: SDT Q600) and the results are shown in Fig. 6. GO shows two major weight losses, the one between 70 and 120 °C of about 22% due to the removal of hydroxyl functional groups present in the sample and the second one around 150–270 °C of about 28% towards the removal of other oxygen functional groups in the GO sample. A gradual loss of 16% of weight from 270 to 1200 °C by liberating the amorphous carbon was observed [37]. The 8% weight losses for the samples GIA1 and GIA3 were observed at 80 °C for the removal of hydroxyl groups, then stable up to 250 °C. Again 44% losses between 250 and 450 °C confirm the presence of silver halides. For the samples GIA2 and GIA4, the first weight loss is about 4% around 80 °C and then the second one between 270 and 430 °C of about 32%. The difference in the weight loss is due to the changes in the composition of AgX and rGO in the samples. In samples GIA2 and GIA4, most of the silver atoms transferred to the silver halide, which results in a high yield compared to GIA1 and GIA3. These results are consistent with the powder XRD patterns of GIA2 and GIA4 that the suppression of the peaks correspond to the Ag phase in these samples, and the rise of the SPR band at around 350 nm is observed in the UV–Vis spectra of GIA1 and GIA3 samples.
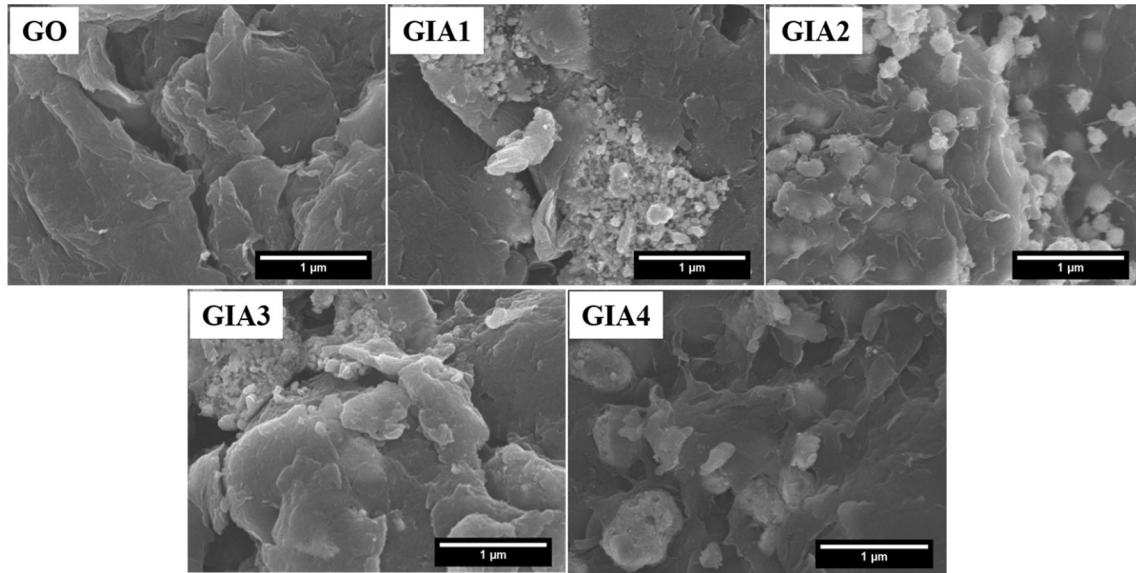

Fig. 4 Micro-Raman spectra of GIA samples

Fig. 5 SEM image of the GO and GIA samples

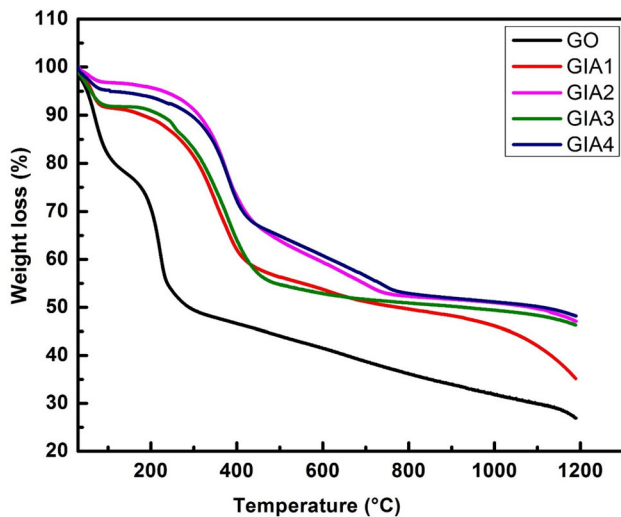Fig. 6 Thermogravimetric analysis of the GIA samples

Fig. 7 Differential scanning calorimetric curves for the GIA samples

DSC measurements performed for the prepared samples are shown in Fig. 7, GO has two peaks at 82 and 231 °C corresponding to the removal of water molecules and oxygen functional groups in GO, respectively [38]. These two peaks are suppressed in other samples due to the reduction of GO. An endothermic peak at 956 °C is for the melting of the metallic silver observed in all GIA samples [39]. For the samples, GIA2 and GIA4, a small endothermic peak present at 414 °C corresponds to the melting of AgX (Br & F). The melting point of pure AgBr is at 430 °C, here it decreased to 414 °C due to the dop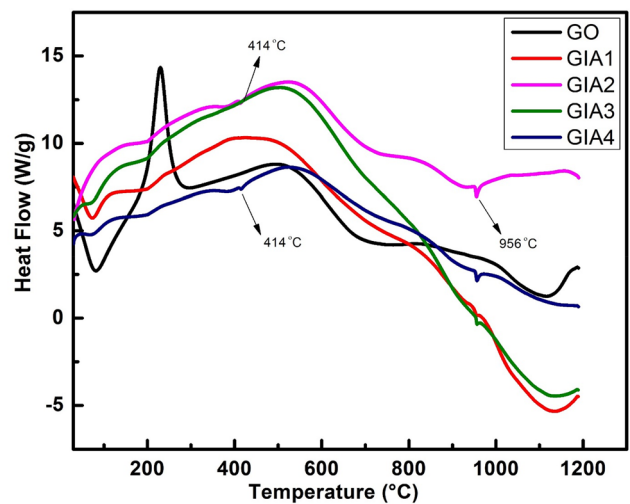ing of F⁻ in the crystal system. In the samples, GIA1 and GIA3, the endothermic peak corresponding to the AgX (Br & F) was not appeared. These results are consistent with the results of TGA that the compositional changes in the products lead to these results.

All the samples have exhibited good photocatalytic activity towards the degradation of MB dye and the results are shown in Fig. 8. Among the four samples, GIA1 and GIA3 have better activity compared to GIA2 and GIA4. This is due to the formation of Ag/AgX which was used to increase the absorption of sunlight. The presence of Ag will increase the visible light absorption through SPR effect, leading to
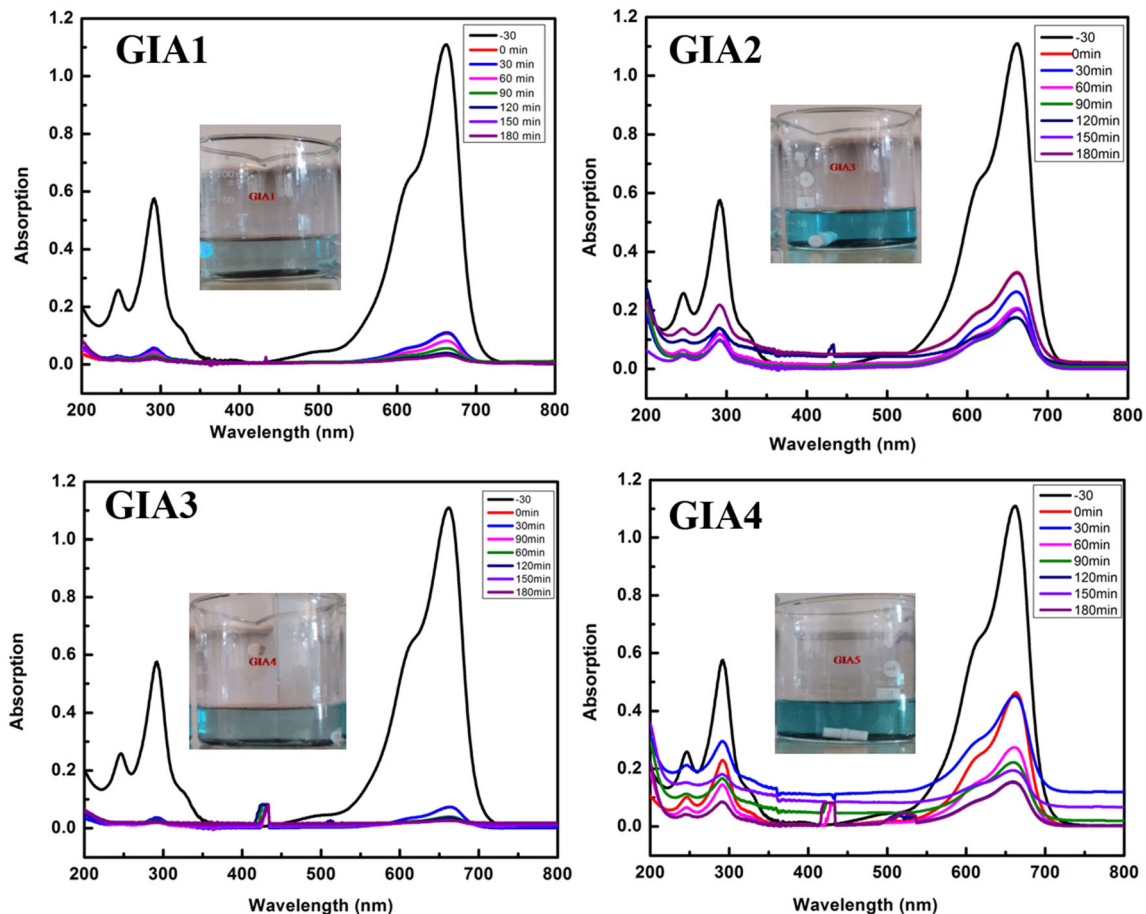
Fig. 8 UV–Vis spectra of the MB dye solution in the presence of GIA composites

increased photocatalytic activity. In the case of GIA2 and GIA4, most of the metallic silver was converted to silver halides, so the surface was covered with AgX which reduced the SPR effect. Another drawback in the AgX samples is the electron–hole recombination. In the above composites, rGO acts as an electron scavenger, due to its more conducting nature, which helps to avoid electron–hole recombination. Restricting the electron–hole recombination was a crucial part in the photocatalytic process.

The photocatalytic degradation was evaluated from the C_o/C curve and is shown in Fig. 9a. The C_o and C are the concentrations of the dye at $t = 0$ and reaction time t. From this curve, one can find the amount of dye present in the solution at a time. The samples GIA1 and GIA3 have the highest degradation efficiency, and at the end of the photocatalytic reaction 3% and 2.5% of dye were present in the solution, respectively. In the case of GIA2 and GIA4, 16% and 14% dye were present in the solution, respectively. The high degradation efficiency of GIA1

and GIA3 is due to the Ag/AgX heterostructure formation.

Based on the above results, the following mechanism is proposed for the photocatalytic degradation of the MB dye by the GIA composites. The superoxide ($\cdot O_2^-$) and the hydroxide radicals ($\cdot OH$) play a crucial role in the degradation of organic dye molecules. The mechanism for the above-prepared composites is shown in Fig. 9b. When the catalyst is subjected to the visible light, AgX gets excited by the absorption of light and creates electron–hole pairs. Silver was excited by the localized SPR effect and produced the polarization of charges. Hence, the polarization of charges was induced by the SPR effect; this polarization-induced electrified field on the Ag–AgX interface separates the electrons far away from the interface. It avoids the electron–hole recombination which should be avoided in the photocatalytic process. Then, the electrons are transferred to the rGO sheets that further separate electrons from the AgX. These conduction band (CB) electrons
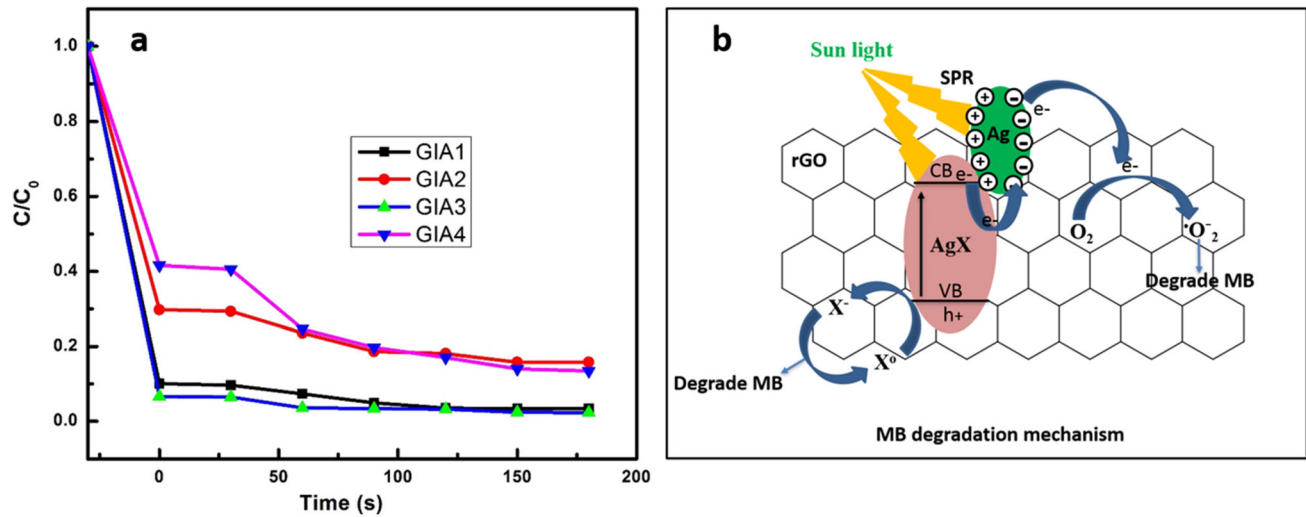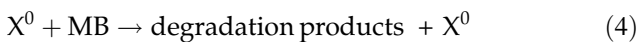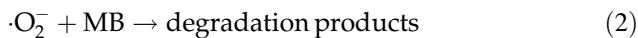
Fig. 9 **a** Photocatalytic degradation of MB and **b** degradation mechanism

transferred through rGO to the surface adsorbed oxygen species converts it in to $\cdot O_2^-$ (superoxide, Eq. 1). This superoxide is involved in the process of MB degradation (Eq. 2), and the reactions are given below:

$$e^- + O_2 \rightarrow \cdot O_2^- \tag{1}$$

$$\cdot O_2^- + MB \rightarrow \text{degradation products} \tag{2}$$

$$h^+ + X^- \rightarrow X^0 \tag{3}$$

$$X^0 + MB \rightarrow \text{degradation products} + X^0 \tag{4}$$

Another degradation mechanism has been carried out by the halide ions (X^-) and is represented in Eqs. 3 and 4, halide ions in the AgX system interact with h^+ in the valence band (VB) giving X^0. Further, these X^o degrade the MB dye [13]. The prepared Ag/AgX-rGO composites have shown high degradation efficiency due to the two-way process, and effective charge separation by rGO. To further analyze the results, the bandgap values for the AgX samples were calculated from the Tauc plot, which is given in (supplementary information) SF 1. The bandgap values are 2.4, 1.4, 2.8, and 1.2 eV for the samples GIA1, GIA2, GIA3, and GIA4, respectively. To understand the photocatalytic mechanism, the conduction band and valance band edges are calculated from the formulas $E_{vb} = \chi - E_c + 0.5 E_g$ and $E_{cb} = E_{vb} - E_g$. Here, χ—work function of the material, E_c—energy of the free electron in hydrogen scale (4.5 eV), E_g = bandgap of the semiconductor, E_{vb}—valance band edge potential, and E_{cb}—conduction band edge potential. The work function for the AgX

samples is calculated as 6 eV. The conduction band edges (valance band edges) for the samples calculated in eV are 0.3 (2.7), 0.8 (2.2), 0.1 (2.9), and 0.8 (2.2) for the samples GIA1, GIA2, GIA3, and GIA4, respectively. Based on the works of literature, the conduction band and valance band edges for the rGO are calculated as -1.8 and 1.8 eV [40, 41]. The e^- and h^+ transitions and the photocatalytic process are explained in Scheme S1 (supplementary information) for the sample GIA1. The electrons produced in the AgX (GIA1 and GIA3) semiconductor after the exposure of the sample in visible light are moved to the Ag metal because its Fermi level is more positive than the conduction band edge of AgX. The h^+ in the AgX sample involved the oxidation reaction and the e^- in the rGO involved the oxidation reactions. In the case of GIA2 and GIA4 samples, the metal silver does not perform the above-said charge separation process, and the photocatalytic efficiency is low compared to the samples GIA1 and GIA3. These mechanisms are consistent with the experimental results.

The results are compared with the previous experimental studies and are given in the following Table 2. The samples show good visible light photocatalytic degradation efficiency with the minimum quantity of the catalysts used.

Table 2 Comparison of photocatalytic degradation properties of the sample with recent literature

Material	Dye	Light source	Catalysts concentration	Degradation		Ref.
				Time (min)	%	
Ag@AgBr/g-C$_3$N$_4$	Methyl orange and Rhodamine B (10 mg L^{-1})	Visible light	100 mg	10	95 & 95	[9]
Ag@AgCl-GO and Ag@AgBr-GO	Acridine orange (20 mg L^{-1}) in 30 mL	Visible light	10 mg	25	95 & 92	[11]
Ag@AgCl-GO and Ag@AgBr-GO	Methyl orange 15 mg L^{-1} and 12 mL	Visible light	7.3 &7.4 mg	40	71 &85	[12]
GN-AgBr	MB (0.6 mM) in 39.2 mL	Visible light	30 mg	50	99	[13]
Ag@AgCl/rGO	Rhodamine B 10 mg L^{-1} of 50 mL	Visible light	50 mg	16	95	[14]
GO/AgBr	MO, RhB & MB 50 micr M L^{-1} in 100 mL	Visible light	100 mg	20	100, 80 & 75	[15]
Ag@AgCl	MO 10 mg L^{-1} in 100 mL	Visible light	20 mg	40	88	[20]
Ag@AgX (Cl & Br)-rGO	MB 5 mg L^{-1} in 100 mL	Visible light	5 mg	150	97.5	Present work

4 Conclusion

In this work, Ag/AgX-rGO-based plasmonic photocatalytic materials were synthesized by using imidazolium-based ILs in a MW-assisted modified polyol process. The formation of Ag/AgX-rGO was confirmed by powder XRD. The presence of 352 nm peak in UV–Vis spectra of GIA1 and GIA3 confirms the presence of Ag. FT-IR, micro-Raman, and FE-SEM analyses show the modifications in the rGO structure and decoration of Ag/AgX nanoparticle over the rGO sheets. The variations in the weight loss percentages of the GIA samples indicate the compositional differences and endothermic peaks at 956 °C showing the presence of Ag. The compositional changes were due to the anion exchange reactions between the ILs and nitrate in the silver nitrate precursor. The photocatalytic activity of the samples was tested by degrading the MB dye under natural sunlight environment. Samples GIA1 and GIA3 showed comparatively higher activity due to the presence of the Ag/AgX in it, the presence of Ag increases the visible light absorption as well as enhances the charge separation by transferring electrons to rGO. Based on the results, it is concluded that by changing the concentration of the ILs we can tune the composition of Ag and AgX which will tune its photocatalytic properties.

References

1. P. Anil Kumar Reddy, P. Venkata Laxma Reddy, E. Kwon, K.H. Kim, T. Akter, S. Kalagara, Environ. Int. **91**, 94–103 (2016)
2. J. Yu, G. Dai, B. Huang, J. Phys. Chem. **113**, 16394–16401 (2009)
3. X. Guo, D. Deng, Q. Tian, Powder Technol. **308**, 206–213 (2017)
4. D. Li, L. Ouyang, L. Yao, L. Zhu, X. Jiang, H. Tang, Chem. Sel. **3**, 428–435 (2018)

5. C. An, J. Wang, W. Jiang, M. Zhang, X. Ming, S. Wang, Q. Zhang, Nanoscale 4, 5646–5650 (2012)

6. P. Wang, B. Huang, X. Zhang, X. Qin, Y. Dai, Z. Wang, Z. Lou, Chem. Cat. Chem. 3, 360–364 (2011)

7. A. Abullzi, K. Kadeer, H. Maimaitizi, Y. Tursun, D. Talifu, Environ. Sci. Pollut. Res. 27, 43615–43624 (2020)

8. S.A. Sher Shah, W.J. Kim, J. Park, D.K. Rhee, I.H. Jamg, N.G. Park, J.Y. Lee, P.J. Yoo, A.C.S. Appl, Mater. Interfaces. 6, 20819–20827 (2014)

9. Y. Yang, W. Guo, Y. Guo, Y. Zhao, X. Yuan, Y. Guo, J. Hazard. Mater. 271, 150–159 (2014)

10. Z. Xu, J. Zhang, H. Liu, P. Kuang, S. Wang, X. Fu, Nano-mater. Nanotechnol. 7, 1–8 (2017)

11. Y. Wang, L. Sun, B. Fugetsu, J. Mater. Chem. A. 1, 12536–12544 (2013)

12. M. Zhu, P. Chen, M. Liu, ACS Nano 5, 4529–4536 (2011)

13. M. Zhu, P. Chen, M. Liu, J. Mater. Chem. 22, 21487–21494 (2012)

14. H. Zhang, X. Fan, X. Quan, S. Chen, H. Yu, Environ. Sci. Technol. 45, 5731–5736 (2011)

15. D. Zhang, H. Tang, Y. Wang, K. Wu, H. Huang, G. Tang, J. Yang, Appl. Sur. Sci. 319, 306–311 (2014)

16. C. Zheng, M. Guo, B. Tian, J. Zhang, Chem. Phys. Lett. 575, 81–85 (2013)

17. C. Janiak, Metal nanoparticle synthesis in ionic liquids. Top. Organomet. Chem. 51, 17–54 (2015)

18. T.Y. Kim, W.J. Kim, S.H. Hong, J.E. Kim, K.S. Suh, Angew. Chem. 121, 3864–3867 (2009)

19. L.Z. Ren, J.X. Wang, Mater. Sci. China. 4, 398–401 (2010)

20. Y. Xu, H. Xu, H. Li, J. Yan, J. Xia, S. Yin, Q. Zhang, Colloids and surfaces A: physicochem. Eng. Aspects. 416, 80–85 (2013)

21. M. Tunckol, J. Durand, P. Serp, Carbon 50, 4303–4334 (2012)

22. A. Chinnappan, R.A. Ntiamoah, W.J. Chung, H. Kim, Int. J. Hydrog. Energy. 41, 14491–14497 (2016)

23. K. Lakshmanamoorthy, S. Manivannan, A.I.P. Con, Proc. 2265, 030710 (2020)

24. J.D. Holbrey, W.M. Reichert, R.P. Swatloski, G.A. Broker, W.R. Pitner, R. Seddon, R.D. Rogers, R. May, Green Chem. 4, 407–413 (2002)

25. W. Wang, L. Shao, W. Cheng, J. Yang, M. He, Catal. Commun. 9, 337–341 (2008)

26. L. Company, B. William, R.E. Offeman, J. Am. Chem. Soc. 89, 1958 (1958)

27. T. Bao, L. Song, S. Zhang, Appl. Organomet. Chem. 32, e4349 (2018)

28. S.W. Kang, K. Char, J.H. Kim, C.K. Kim, Y.S. Kang, Chem. Mater. 16, 1789–1794 (2006)

29. I. Dinares, C.G. de Miguel, A. Ibanez, N. Msquida, E. Alcalde, Green Chem. 11, 1507–1510 (2009)

30. P. Naert, K. Rabarey, C.V. Stevens, Green Chem. 20, 4277–4286 (2018)

31. B. Kumar Barman, K. Kar Nanda, RSC Adv. 4, 44146–44150 (2014)

32. B. Anis, A.M. Mostafa, Z.A. El Sayed, A.S.G. Khalil, A. Abouelsayed, Opt. Laser Technol. 103, 367–372 (2018)

33. Y.J. Song, M. Wang, X.Y. Zhang, J.Y. Wu, T. Zhang, Nanoscale Res. Lett. 9(17), 2–8 (2014)

34. R. Bryaskova, D. Pencheva, S. Nikolov, T. Kantardjiev, J. Chem. Biol. 4, 185–191 (2011)

35. T. Kavinkumar, D. Sastikumar, S. Manivannan, RSC Adv. 5, 10816–10825 (2015)

36. A. Kaniyoor, S. Ramaprabhu, AIP Adv. 2, 032183–032183 (2012)

37. S. Jin, Q. Gao, X. Zeng, R. Zhang, K. Liu, X. Shao, M. Jin, Diam. Relat. Mater. 58, 54–61 (2015)

38. V. Patil, R.V. Dennis, T.K. Rout, S. Banerjee, G.D. Yadav, RSC Adv. 4, 49264–49272 (2014)

39. S. Kota, P. Dumpala, R.K. Anantha, M.K. Verma, S. Kandepu, Sci. Rep. 7, 11566 (2017)

40. J. Mangalam, M. Kumar, M. Sharma, M. Joshi, Nano-Struct. Nano-Objects 17, 58–66 (2019)

41. J. Liu, M. Durstock, L. Dai, Energy Environ. Sci. 7, 1297–1306 (2014)

Springer